

Unveiling the Interlayer Spacing Dependence of Zn-Ion Storage Performance in Layered Vanadium Phosphates

Linfeng Hu (✉ linfenghu@seu.edu.cn)

Southeast University <https://orcid.org/0000-0002-0640-508X>

Zeyi Wu

Fudan University

Chengjie Lu

Southeast University

Fei Ye

Southeast University

Ruilvjing Pang

Southeast University

Yang Liu

Southeast University

Zhengming Sun

Southeast University

Article

Keywords: phenylamine-intercalation, VOP₀4·2H₂O, interlayer spacing, diffusion kinetics, electrochemical stability, aqueous Zinc-ion battery

Posted Date: March 10th, 2021

DOI: <https://doi.org/10.21203/rs.3.rs-258081/v1>

License: © ⓘ This work is licensed under a Creative Commons Attribution 4.0 International License.

[Read Full License](#)

Unveiling the Interlayer Spacing Dependence of Zn-Ion Storage Performance in Layered Vanadium Phosphates

Linfeng Hu^{*1,2,3}, Zeyi Wu^{2,3}, Chengjie Lu¹, Fei Ye¹, Ruilvjing Pang¹, Yang Liu¹, Zhengming Sun¹

1. School of Materials Science and Engineering, Southeast University, Nanjing, 211189, China

2. Department of Materials Science, Fudan University, Shanghai 200433, China

3. These authors contributed equally: Linfeng Hu, Zeyi Wu

** Address correspondence to: linfenghu@seu.edu.cn*

Abstract

Layered vanadium phosphate ($\text{VOPO}_4 \cdot 2\text{H}_2\text{O}$) is reported as a promising cathode material for rechargeable aqueous Zn^{2+} batteries (ZIBs) owing to its unique layered framework and high discharge plateau. However, its sluggish Zn^{2+} diffusion kinetics, the low specific capacity and poor electrochemical stability remains a major issue in battery application. In this work, a group of phenylamine (PA)-intercalated $\text{VOPO}_4 \cdot 2\text{H}_2\text{O}$ with varied interlayer spacing (14.8, 15.6 and 16.5 Å) is synthesized respectively via a solvothermal method for cathode of aqueous ZIBs. The specific capacity is quite dependent on d -spacing in PA- $\text{VOPO}_4 \cdot 2\text{H}_2\text{O}$ system followed by an approximate linear tendency, and the maximum interlayer spacing (16.5 Å phase) results in a discharge capacity of 268.2 $\text{mAh} \cdot \text{g}^{-1}$ at 0.1 $\text{A} \cdot \text{g}^{-1}$ with a high discharge plateau of ~ 1.3 V and an energy density of 328.5 $\text{Wh} \cdot \text{Kg}^{-1}$. Both of the experimental data and DFT calculation identify that the optimal 16.5 Å spacing can boost fast Zinc-ion diffusion with an ultrahigh diffusion coefficient of $\sim 5.7 \times 10^{-8} \text{ cm}^2 \cdot \text{s}^{-1}$. The intercalation of PA molecules also significantly increases the hydrophobicity in the aqueous electrolyte, resulting in the inhibiting the decomposition / dissolution of $\text{VOPO}_4 \cdot 2\text{H}_2\text{O}$ and remarkably improved cycling stability over 2000 cycles at 5.0 $\text{A} \cdot \text{g}^{-1}$ with a capacity retention of $\sim 200 \text{ mAh} \cdot \text{g}^{-1}$. Our study provides a feasible solution on the sluggish Zn^{2+} diffusion kinetics and poor cyclstability, and also shows a clear understanding on the interlayer chemistry of layered phosphates towards aqueous Zinc-ion storage.

Keywords:

phenylamine-intercalation; $\text{VOPO}_4 \cdot 2\text{H}_2\text{O}$; interlayer spacing; diffusion kinetics; electrochemical stability; aqueous Zinc-ion battery

Nowadays, although rechargeable lithium-ion batteries (LIBs) are widely used for various portable electronics and electric vehicles, limited Li sources and severe safety issue are two main drawbacks of LIBs. With the rapid development of modern electronics and advanced equipments, beyond-lithium-ion (Na^+ , K^+ , Mg^{2+} , Ca^{2+} , Zn^{2+} , Al^{3+}) batteries have recently attracted growing attention for energy storage systems.¹ Among them, Zinc is abundant metallic elements in the earth crust far exceeding Li. More importantly, rechargeable aqueous Zinc-ion batteries (ZIBs) are based on aqueous electrolyte, resulting in much superior safety than that of alkali metal (Li^+ , Na^+ , K^+) based secondary batteries. Consequently, ZIBs have been considered as very promising candidates for next-generation battery systems.^{2,3} Nevertheless, the revolution of aqueous ZIBs is still at the early stage and far from the prospective applications, which is mainly limited by the absence of suitable cathode materials especially with high energy density and sufficient long lifespan.⁴ The origin of this issue should be ascribed to the intrinsic difference between univalent lithium ion and divalent zinc ion. Since the similar radius of Li^+ (0.076 nm) and Zn^{2+} (0.074 nm), the surface charge density of divalent Zn^{2+} is more than the twice of Li^+ , and the much stronger electrostatic interaction between Zn^{2+} and lattice framework of the electrode materials thus leads to sluggish diffusion kinetics and even structure deterioration.^{5,6}

Inorganic layered compounds, based on a typical layered structure and rich intercalation chemistry, have been particularly studied in metal-ion batteries. Especially, layered vanadium phosphate, $\text{VOPO}_4 \cdot 2\text{H}_2\text{O}$, has been reported as an important cathode material for ZIBs accompanied with a Zn^{2+} intercalation / de-intercalation mechanism in its interlayer galleries.⁷⁻⁹ Remarkably, taking advantage of the enhanced ionicity of V-O bonds with the existence of PO_4^{3-} , layered $\text{VOPO}_4 \cdot 2\text{H}_2\text{O}$ exhibits a much higher discharge plateau (1.1 - 1.2 V) than other V-based cathode materials.¹⁰⁻¹² It should be emphasized that energy density is quite dependent on the discharge plateau of cathode, and such a merit of layered $\text{VOPO}_4 \cdot 2\text{H}_2\text{O}$ is highly desirable to achieve high energy density of ZIBs.¹⁰ Unfortunately, the specific capacity, rate capability of $\text{VOPO}_4 \cdot 2\text{H}_2\text{O}$ -based ZIBs is still unsatisfied due to the strong electrostatic interactions between Zn^{2+} and VOPO_4 host with sluggish Zn^{2+} diffusion kinetics. On the other hand, the dissolution / decomposition behavior of $\text{VOPO}_4 \cdot 2\text{H}_2\text{O}$ in mild aqueous electrolyte generally results in very fast capacity / voltage fading during long-term cycling with a rather poor cyclability. Although the dissolution / decomposition issue has been addressed by PO_4^{3-} addition and high salt concentration of the aqueous electrolyte to the shift the decomposition equilibrium and prevent dissolution⁹, the as-reported capacity of $\text{VOPO}_4 \cdot 2\text{H}_2\text{O}$ cathode is still less

than $170 \text{ mAh}\cdot\text{g}^{-1}$, which is much smaller than its theoretical specific capacity ($>300 \text{ mAh}\cdot\text{g}^{-1}$). It is still a challenge to realize the superior performances for layered $\text{VOPO}_4\cdot 2\text{H}_2\text{O}$ combining high discharge capacity, high rate capability and long cycling stability toward aqueous ZIBs applications.

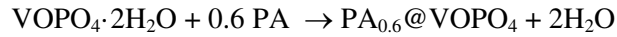
Recent progress on lithium- / sodium- / magnesium-ion batteries unveils the interlayer spacing of layered materials as natural two-dimensional (2D) ion transport / diffusion channels.¹³⁻¹⁶ In principle, increasing the interlayer spacing of layered structure facilitates the ion transport by creating a lower energy barrier.^{6,17,18} Superior battery performance should be explored from the layered materials with larger interlayer spacing. As well, it is of great interest to make a fundamental understanding of the dependence of Zinc-ion storage behaviour on interlayer spacing for layered $\text{VOPO}_4\cdot 2\text{H}_2\text{O}$. However, it is still no report on the interlayer spacing modulation in layered vanadium phosphate up to date.

Herein, we found that the interlayer spacing of layered $\text{VOPO}_4\cdot 2\text{H}_2\text{O}$ (VOP, 7.4 \AA) can be successfully tuned by a phenylamine (PA) intercalated strategy through a facile solvothermal route. The crystal water in the $\text{VOPO}_4\cdot 2\text{H}_2\text{O}$ was extracted from the interlayer space accompanied with the PA molecules intercalation. Three PA-intercalated VOPO_4 (labeled as PA-VOP) phases with identical *d*-spacing (16.5 \AA , 15.6 \AA and 14.8 \AA) has been respectively achieved (Fig. 1a). We revealed an approximate linear dependence of the capacity dependence on interlayer spacing, and the maximum interlayer spacing (16.5 \AA phase) results in a discharge capacity of $268.2 \text{ mAh}\cdot\text{g}^{-1}$ at $0.1 \text{ A}\cdot\text{g}^{-1}$ and an energy density of $328.5 \text{ Wh}\cdot\text{Kg}^{-1}$. More importantly, the PA intercalation also significantly increases the hydrophobicity in the aqueous electrolyte, resulting in inhibition of the decomposition / dissolution of $\text{VOPO}_4\cdot 2\text{H}_2\text{O}$ and remarkably improved cycling stability over 2000 cycles with a capacity retention of $\sim 200 \text{ mAh}\cdot\text{g}^{-1}$ at $5.0 \text{ A}\cdot\text{g}^{-1}$.

Results

Controllable PA intercalation. Uniform $\text{VOPO}_4\cdot 2\text{H}_2\text{O}$ (JCPDS: 36-1472, labeled as VOP) nanoplates were first obtained by a conventional refluxing method reported previously.¹¹ After a rapid solvothermal treatment of the as-prepared $\text{VOPO}_4\cdot 2\text{H}_2\text{O}$ nanoplates in PA-contained isopropanol solvent at $60 \text{ }^\circ\text{C}$ for 2 h, the sharp (001) peak of pristine $\text{VOPO}_4\cdot 2\text{H}_2\text{O}$ substantially shifted to a lower angle (5.3°) with much decreased intensity (Fig. 1b), corresponding to an extreme increase in basal spacing up to 16.5 \AA with simultaneously reduced crystallinity during the intercalation. Fourier transform infrared spectroscopy (FTIR) reveals the presence of $\nu(\text{N-H})$, $\nu(\text{C-H})$, $\delta(\text{C-H})$ vibration mode and featured peak of benzene ring (Fig. 1c), demonstrating the successful intercalation of phenylamine molecules.^{19,20} It is

noteworthy that the characteristic peaks of crystal water in precursor $\text{VOPO}_4 \cdot 2\text{H}_2\text{O}$ completely disappear in FTIR spectrum after PA-intercalation. Thermogravimetric analysis (TGA) (Supplementary Fig. 1) identifies a weight loss of 25.3 % of PA-VOP up to 400 °C, corresponding to 0.6 unit phenylamine molecule contained in one unit PA-VOP structure. These results implies the phenylamine molecules replace the crystal water in $\text{VOPO}_4 \cdot 2\text{H}_2\text{O}$ interlayer to well maintain the initial layered framework as follows:



Scanning electron microscope (SEM) observations show an edge-crimped plate like morphology with lateral size of 5 to 20 μm and increased thickness feature compared to precursor VOP (Fig. 1d, Supplementary Fig. 2). However, transmission electron microscope (TEM) and atomic force microscopy (AFM) characterizations suggest a much smaller thickness of $\sim 30 \text{ nm}$ for our PA-VOP sample (Supplementary Fig. 3, Fig. 4). We consider that such a thickness difference should be caused by the possible liquid-exfoliation during the ultrasonic treatment of the sample preparation for TEM/AFM observation. Especially, one can clearly distinguish an interlayer spacing of $\sim 1.6 \text{ nm}$ from the cross-sectional high-resolution transmission electron microscope (HRTEM) image (Supplementary Fig. 4), which is well agreed with the one detected from the XRD data in Fig. 1b. Energy dispersive spectrum (EDS)-mapping profiles further clarify the uniform distribution of V, P, O, C, N elements after PA intercalation (Supplementary Fig. 4).

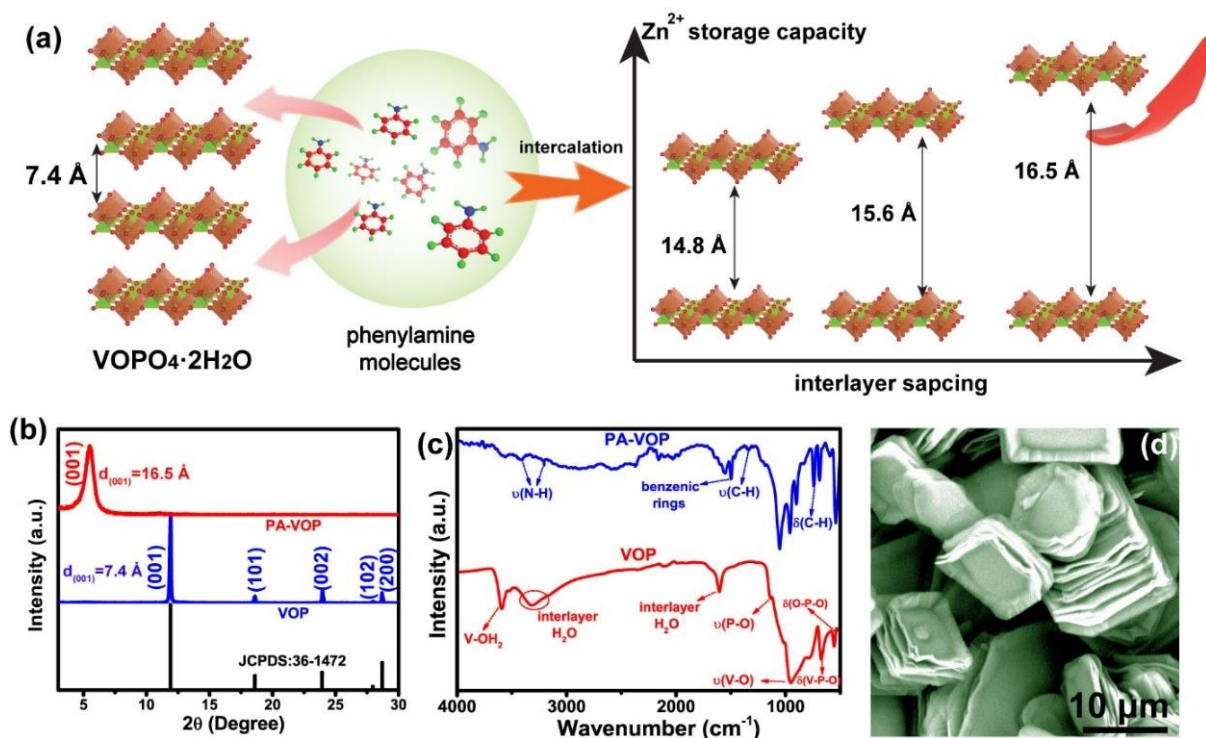


Fig. 1 Controllable PA intercalation in layered $\text{VOPO}_4 \cdot 2\text{H}_2\text{O}$. **a** Scheme of capacity regulation for Zinc-ion storage via PA-intercalation engineering. **b** Powder XRD patterns and **c** FTIR spectra of VOP and PA-VOP samples, respectively. **d** Typical SEM image of PA-VOP (16.5 Å phase).

Interlayer spacing dependence of Zn-ion storage. Interestingly, we found the interlayer spacing of the PA-intercalated samples can be carefully tuned by solvothermal time. Three PA-VOP samples with different interlayer spacing of 14.8, 15.6 and 16.5 Å can be obtained under well-controlled solvothermal time of 60, 90 and 120 min, respectively (Fig. 2a). A further increase of solvothermal time compromises the interlayer spacing, indicating a saturated intercalation reaction at this threshold time (Fig. 2b). TGA curves suggests the weight loss of PA-VOP (14.8 Å), PA-VOP (15.6 Å) and PA-VOP (16.5 Å) is 19.1 %, 21.3 % and 24.5 % from 140 to 380 °C, respectively (Supplementary Fig. 5). Thus, it is rational that the increase of interlayer spacing is attributed to higher content of intercalated phenylamine molecules upon prolonging reaction time.²¹ Note that the as-obtained interlayer spacing of 16.5 Å in our work is the maximal one among all of the reported layered cathodes for aqueous ZIBs such as layered $\delta\text{-MnO}_2$, PA-MnO₂ and $\text{Zn}_{0.25}\text{V}_2\text{O}_5 \cdot n\text{H}_2\text{O}$ (Fig. 2c).^{7,12,22-28} SEM observation demonstrates the analogous plate-like morphology of the three PA-VOP samples other than a remarkably increased thickness caused by phenylamine insertion (Fig. 2d-f, Fig. 1d).

CR2032 coin cells were then assembled employing these PA-VOP samples as cathode material, Zn foil as anode and 2M $\text{Zn}(\text{CF}_3\text{SO}_3)_2$ solution as aqueous electrolyte, respectively. Typical cyclic voltammetry (CV) curves of Zn // PA-VOP (16.5 Å phase) battery reveals a general active process in the first scan cycle, while the curves of the stabilized second and third cycle gives a pair of oxidation / reduction peak located at around 1.6 V and 1.3 V, respectively (Supplementary Fig. 6). It is should be noteworthy that PA molecules is generally inactive in mild aqueous electrolyte, and the electrochemical activity and capacity contribution should be mostly provided from VOPO_4 framework.²⁹⁻³¹ The galvanostatic charge discharge (GCD) curves also exhibit steady charge and discharge plateaus with well agreement with the voltage range in CV curves (Supplementary Fig. 6, 7). It has been reported that non-metal proton (H^+) has also been recognized as charge carrier ions for some aqueous batteries.³² To clarify this, we compare the electrochemical performance on both aqueous and non-aqueous system (0.5 M ZnSO_4 / acetonitrile, Supplementary Fig. 8). No apparent difference has been observed between the CV peaks, thereby ruling out the possible contribution from proton intercalation in our system. *Ex-situ* XRD at different voltages in the second cycle reveals a revisable Zn^{2+} intercalation / de- intercalation mechanism of the PA-VOP cathode (Supplementary Fig. 9). We found the specific capacity of the PA-VOP cathodes is quite dependent on its interlayer spacing. As shown in Fig. 2g, the pristine VOP (7.4 Å) and the PA-VOP samples (14.8 Å phase, 15.6 Å phase and 16.5 Å phase) delivers a discharge capacity of 138.4 $\text{mA}\cdot\text{g}^{-1}$, 226.5 $\text{mAh}\cdot\text{g}^{-1}$, 243.7 $\text{mAh}\cdot\text{g}^{-1}$, and 268.2 $\text{mAh}\cdot\text{g}^{-1}$, respectively. Similar enhancement tendency has been also observed for rate-capacity of series layered phosphates as shown in Fig. 2h. The resultant 16.5 Å phase delivers the maximum rate capability (Fig. 2i): a high specific capacity of 268.2, 254.8, 236.4, 220.7, 207.2, 187.5 $\text{mAh}\cdot\text{g}^{-1}$ has been respectively realized at the current density of 0.1, 0.5, 1.0, 2.0, 5.0, 10.0 $\text{A}\cdot\text{g}^{-1}$ with a recovered capacity of 253.3 $\text{mAh}\cdot\text{g}^{-1}$ when the applied current density turned back to 0.1 $\text{A}\cdot\text{g}^{-1}$.

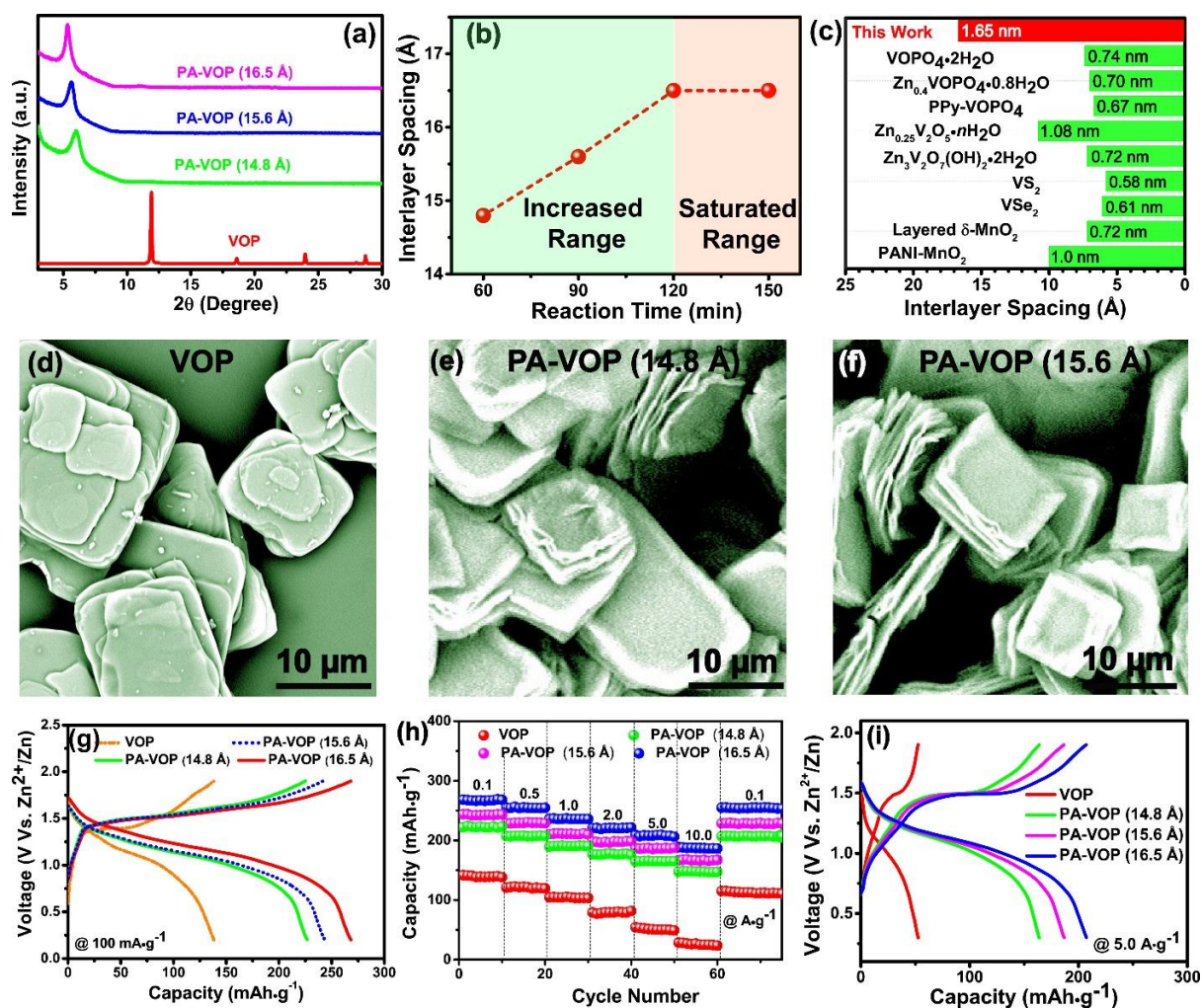


Fig. 2 Interlayer spacing dependent battery performance. **a** XRD patterns of various PA-VOP samples synthesized under different temperature and solvent. **b** Dependence of interlayer spacing and solvothermal time. **c** Typical layered materials served as cathode of aqueous ZIBs.^{7,12,22-28} **d-f** SEM image of VOP, PA-VOP (14.8 Å phase) and PA-VOP (15.6 Å phase) samples, respectively. **g** GCD curves of VOP based ZIB and PA-VOP based ZIBs with adjustable interlayer spacing, respectively (14.8, 15.6 and 16.5 Å). **h** Cycle test at varied current density of VOP and PA-VOP cathodes with different interlayer spacing, severally. **i** GCD curves of VOP and PA-VOP cathode with different interlayer spacing at a current density of 5 A·g⁻¹, respectively.

We reveal the capacity-interlayer spacing dependence could be followed by an approximate linear trend as summarized in Fig. 3a. The specific capacity of 16.5 Å phase (268.2 mAh·g⁻¹) at the current density of 0.1 A·g⁻¹ is about two times higher than that of pristine VOP (138.4 mAh·g⁻¹) and also well above that of layered PPy-VOPO₄ cathode (~ 80 mAh·g⁻¹) reported before.²³ Meanwhile, one can see a voltage plateau versus specific capacity diagram for mainstream cathodes of aqueous ZIBs reported in

recent years (V-based oxides,^{5,17,24,25,33-39} Mn-based compounds,⁴⁰⁻⁴² Prussian Blue analogs,⁴³⁻⁴⁵ polyanion compounds,^{7,22,23,46-48} organics^{29,49-52} and other chalcogenides^{6,26,28,53}) shown in Fig. 3b. Benefited from *d*-spacing dependent performance as shown above, it is evident that rate-capacity of our optimal PA-VOP sample (16.5 Å phase) surpasses most traditional materials including Mn-based oxides (α -MnO₂,⁵⁴ Mn₂O₃,⁴⁰), V-based compounds (Na₃V₂(PO₄)₃,⁴⁶ Zn₃V₂O₇(OH)₂·2H₂O²⁵) and Co₃O₄⁵³ reported recently (Fig. 3c). Taking advantage of its high specific capacity of 268.2 mA·g⁻¹ and prominent discharge plateau (~ 1.3 V), the 16.5 Å-phase PA-VOP renders a high energy density of 328.5 Wh·Kg⁻¹ at a power density of 122.6 W·Kg⁻¹, having apparent advantages in contrast with various popular cathode materials such as V₃O₇·*n*H₂O,³⁵ α -MnO₂,⁵⁵ δ -MnO₂,²⁷ ZnMn_{1.86}O₄,⁴¹ ZnHCF⁴³ and CuHCF (Fig. 3d).⁵⁶ This excellent energy and powder densities promote the application in flexible and wearable electronic devices (Insert in Fig. 3d).

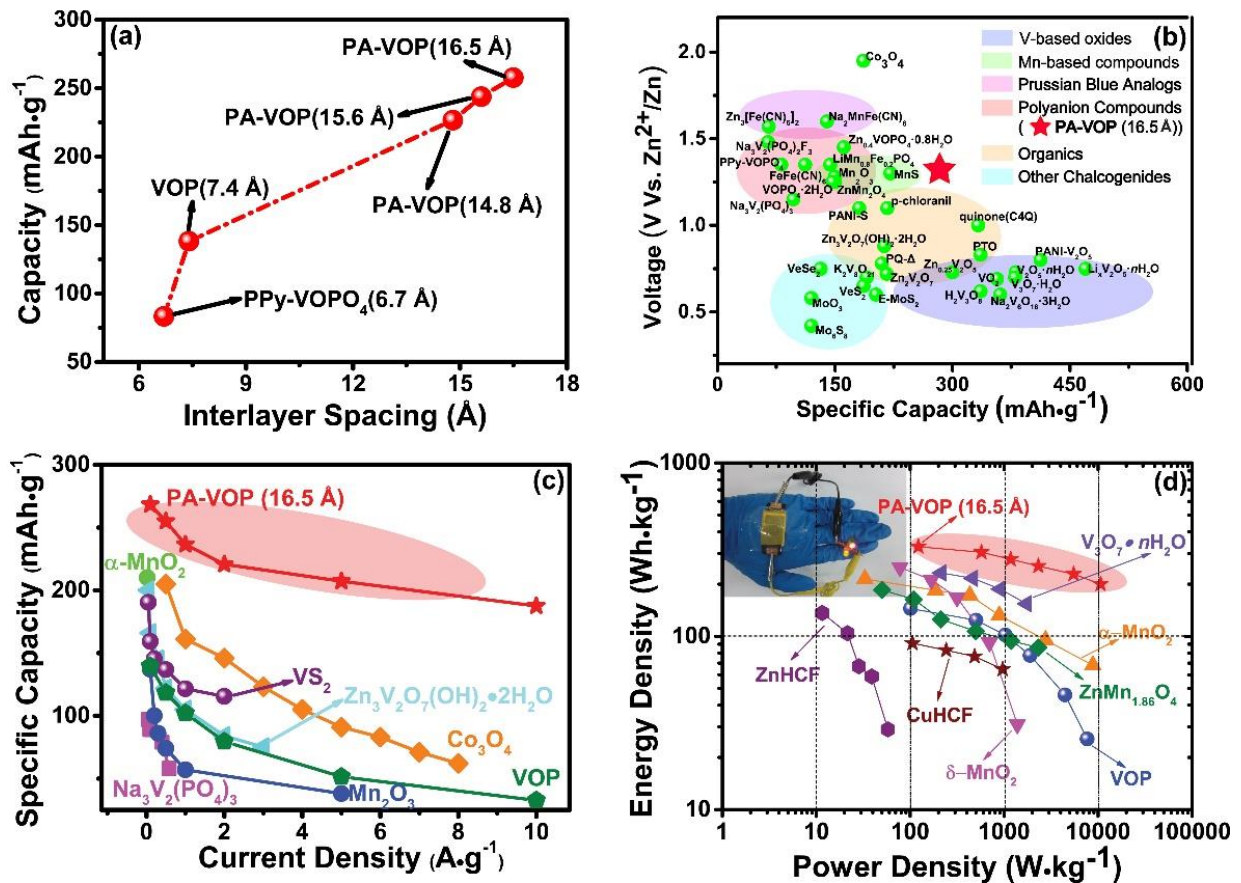


Fig. 3 Performance comparison. **a** Dependence of specific capacity and interlayer spacing of various VOPO₄-based cathodes at the current density of 0.1 A·g⁻¹.²³ **b** Voltage plateau versus specific capacity for various mainstream cathodes recently reported and our PA-VOP (16.5 Å) cathode.^{5-7,17,22-26,33-53} **c** Comparison of the rate-capacity between our PA-VOP cathode and the other recently reported cathodes

for aqueous ZIBs.^{25,40,46,53-54} **d** Ragone plot of PA-VOP cathode and a series of other cathode materials reported previously.^{27,35,41,43,55-56} Insert is a solid-state battery constructed from the PA-VOP @ CFC cathode driving a group of LEDs.

Reaction/diffusion kinetics mechanism. In order to clarify the aforementioned *d*-spacing dependent battery-performance, corresponding study on electronic conductivity and Zinc-ion diffusion kinetics is further conducted. Four-probe conductivity test shows a 2 ~ 7 times higher electronic conductivity of PA-VOP (16.5 Å) in contrast to that of pristine VOP with pressure increased, which is mainly attributed to the intrinsic high conductivity of phenylamine (Fig. 4a). CV curves at varied scan rates are employed to distinguish the capacitive / ion diffusion contribution by analyzing the dependence of the logarithm of peak current density and the scan rate (Supplementary Fig. 10). Theoretically, the peak current (*i*) and sweep rate (*v*) in CV curve follows the rule as:^{57,58}

$$i = a v^b \quad (1)$$

Where *a* and *b* are adjustable values. *b* value of 0.5 indicates a semi-infinite diffusion mechanism, while *b* value of 1.0 suggests capacitive behavior. In our case, *b* value for the predominant peaks of VOP, PA-VOP (14.8 Å phase) and PA-VOP (16.5 Å phase) cathode is determined to be 0.63, 0.73 and 0.76, respectively (Supplementary Fig. 10). Apparently, the capacitive contribution in PA-VOP (16.5 Å phase) cathode is 44.8 %, 49.6 %, 56.7 %, 60.4 %, and 65.9 % at the scan rate of 0.1, 0.2, 0.5, 0.8, and 1.0 mV·s⁻¹, respectively. These values is much higher than that in VOP cathode (28.4 %, 33.2 %, 38.9 %, 42.8 %, and 47.5 % at 0.1, 0.2, 0.5, 0.8, and 1.0 mV·s⁻¹, respectively) (Fig. 4b, c).

On the other hand, Zinc-ion diffusion kinetics is further identified by galvanostatic intermittent titration technique (GITT) (Fig. 4d). Strikingly, an ultrahigh Zinc-ion diffusion coefficient of ~ 5.7 × 10⁻⁸ cm²·s⁻¹ has been detected in 16.5 Å phase, nearly 5 orders of magnitude higher than that of pristine VOP cathode (6.2 × 10⁻¹³ cm²·s⁻¹) and also much higher than that of conventional cathode materials reported recently including V₂O₅, ZnMn₂O₄, Zn₃V₂O₇(OH)₂·2H₂O, and K₂V₈O₂^{25,37,41,59} (Fig. 4e). This drastic increase demonstrates a great improvement in terms of Zn²⁺ intercalation / de-intercalation kinetics by an enlarged 2D interlayer channel as illustrated in Fig. 4f. In principle, large Zinc-ion diffusion coefficient is generally observed in ultrathin samples due to the shortened effective diffusion path and larger activated surface, which drastically facilitate Zn²⁺ diffusion and charge transfer.^{28,60,61} Our previous study also confirms fast Zn-ion diffusion ability in 6.0-nanometer ultrafine spinel oxide

nanodots.⁶¹ However, in the present study, the as-obtained 16.5 Å phase show a significant increase on thickness compared with the pristine VOP sample (Fig 2d-f). Therefore, the thick samples display much faster kinetics than that of thin VOP nanoplates unusually.^{60,62} Such an phenomenon should indicate the Zinc-ion transport in our layered phosphate series is dominated by interlayer diffusion on account of the enlarged interlayer spacing would provide high-efficiency 2D ion diffusion / hopping channels.

Besides, density functional theory (DFT) based first-principle simulation is conducted for a deeper understanding of the greatly improved diffusion kinetics. Climbing-image nudged elastic band (CI-NEB) method is adopted to reveal the possible diffusion paths and the corresponding energy barrier of zinc-ion. The interlayer site on the top of the corner-shared oxygen atom of [PO₄] tetrahedron and [VO₆] octahedron gives an optimal absorption energy of 0.07 eV, which can be determined as the potential adsorption site (called as C site) for zinc-ion diffusion. The as-optimized diffusion path denotes hopping process through the right above site of [VO₆] octahedron and [PO₄] tetrahedron between the adjacent C sites (Fig. 4g, h). Subsequently, an interlayer-dependent activation energy decrease tendency is derived based on such a diffusion path. The energy barrier for zinc-ion diffusion in VOP bulk (7.4 Å) is calculated to be 0.13 eV, and dramatically decreases to a much lower value (~0.03 eV) until a threshold interlayer spacing of 9.7 Å. Further increase of spacing gives rise to a slight change of energy barrier, and it finally decrease to $\sim 2.3 \times 10^{-4}$ eV for PA-VOP (16.5 Å phase) sample. Consequently, the greatly enhanced diffusion kinetics, predominant capacitive contribution and high electronic conductivity in PA-VOP samples provide the essential insight for the interlayer spacing dependent Zn²⁺ storage performance.

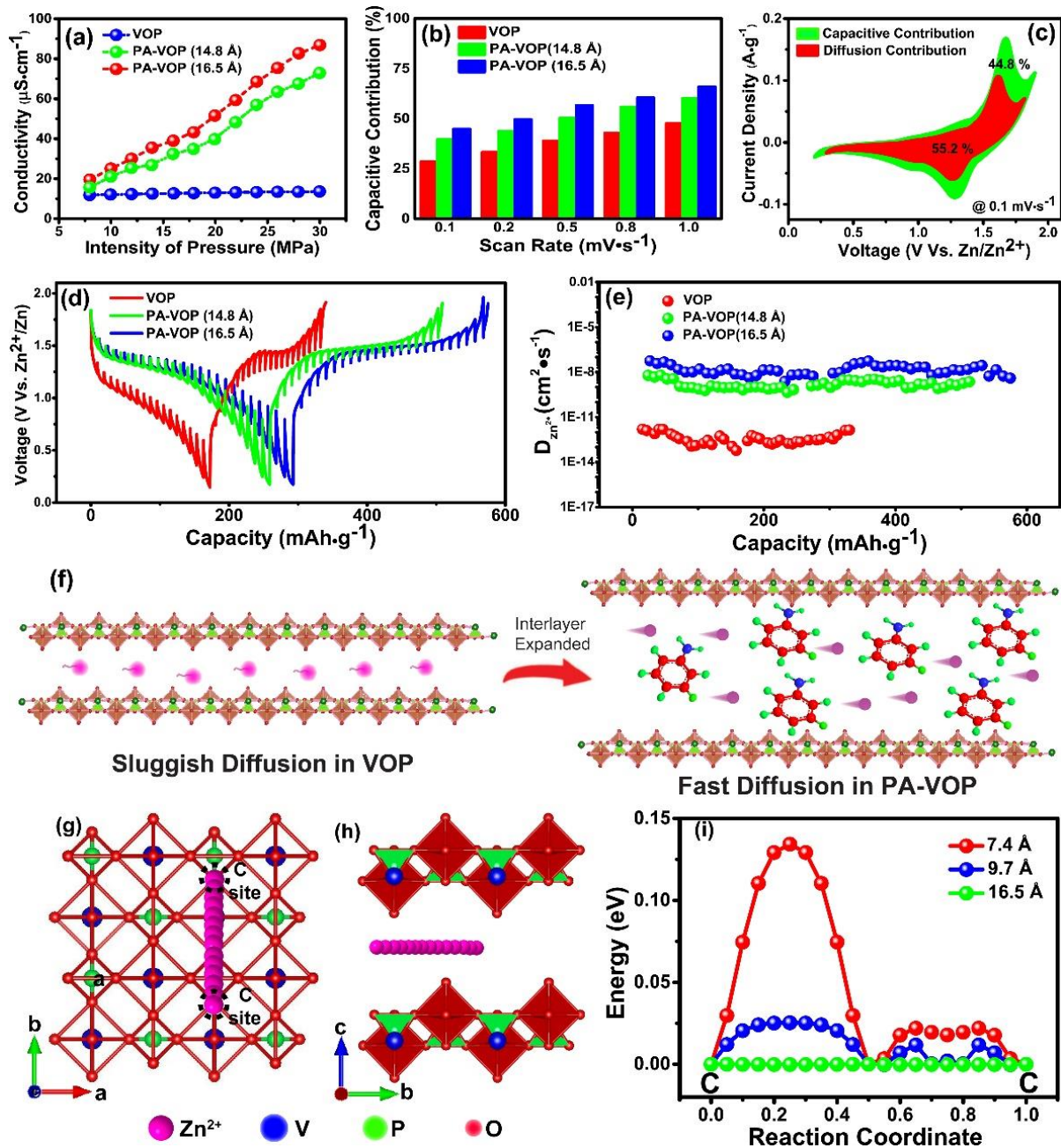


Fig. 4 Reaction/diffusion kinetics mechanism. **a** Electronic conductivity test under different pressure. **b** Capacitive contribution of VOP, PA-VOP (14.8 Å phase) and PA-VOP (16.5 Å phase), respectively. **c** CV curve containing the schematic of capacitive and diffusion contribution of PA-VOP (16.5 Å phase) cathode at the scan rate of $0.1 \text{ mV}\cdot\text{s}^{-1}$ **d** GITT curve and **e** the calculated diffusion coefficient of VOP, PA-VOP (14.8 Å phase) and PA-VOP (16.5 Å phase), respectively. **f** Schematic illustration of Zn^{2+} diffusion kinetics in PA-VOP and VOP cathode. **g** Zinc-ion diffusion path scheme in top view and **h** side view mode. **i** Calculated energy barrier curve of the PA-VOP samples with different interlayer spacing.

Cyclability improvement. It is known that layered $\text{VOPO}_4 \cdot n\text{H}_2\text{O}$ cathode undergoes severe capacity / voltage fading with rather poor cyclability originated from the decomposition / dissolution of $\text{VOPO}_4 \cdot n\text{H}_2\text{O}$ in mild aqueous electrolyte.⁹ Interestingly, we found the chemical stability and electrochemical reversibility was significantly enhanced after the PA intercalation. Compared to aqueous $\text{Zn}(\text{SO}_4)_2$ electrolyte, superior lifespan was observed in $\text{Zn}(\text{CF}_3\text{SO}_3)_2$ electrolyte due to the better desolvation effect of bulky $(\text{CF}_3\text{SO}_3)^-$ versus $(\text{SO}_4)^{2-}$ (Supplementary Fig. 11). One can see the $\text{Zn} // 2\text{M Zn}(\text{CF}_3\text{SO}_3)_2 // \text{PA-VOP}$ (16.5 Å phase) battery delivers an initial specific capacity of 200.9 $\text{mAh} \cdot \text{g}^{-1}$ and a steady cycle stability of 92.3 % capacity retention after 2,000 cycles under a high current density of 5.0 $\text{A} \cdot \text{g}^{-1}$. In contrast, the VOP based battery just exhibits an inferior capacity of ~ 60 $\text{mAh} \cdot \text{g}^{-1}$ with rapid decay in the first 300 cycles (Fig. 5a). To clarify the actual mechanism, *ex-situ* XRD characterizations of VOP and PA-VOP (16.5 Å phase) cathode before and after 300 cycles are carried out as shown in Fig. 5b. Apparently, the characteristic diffraction peaks of VOP cathode completely disappear after 300 cycles, indicating the phase conversion of VOP during the long-term cycling. In contrast, the PA-VOP (16.5 Å phase) cathode well maintained the initial phase without any impurity diffraction peaks. SEM observation also reveals PA-VOP (16.5 Å phase) sample well maintain the initial plate-like morphology compared to the drastic aggregation of VOP cathode after 300 cycles (Fig. 5c). All results demonstrate the greatly enhanced structural reversibility of our PA-VOP sample after PA intercalation.

To further probe the origin of the remarkable difference on long-lifespan, we compare the chemical stability of both VOP and PA-VOP samples in aqueous 2M ZnSO_4 electrolyte. As shown in Fig. 5d, it is clear that VOP sample generally disappears in the bottom of solution followed by a typical color change into deep red after 5 days due to the decomposition /dissolution of $\text{VOPO}_4 \cdot n\text{H}_2\text{O}$ into $\text{VO}_x(\text{s})$ and PO_4^{3-} .⁹ However, the PA-VOP (16.5 Å phase) sample still floats on the liquid surface with much better stability after 5 days (Fig. 5d). Such a result inspires our consideration on the difference on surface-wettability of these two samples. Accordingly, Fig. 5e compares the water-based contact angle on the surface of pressed powder of VOP and PA-VOP sample. The PA-VOP and VOP sample shows a contact angle of 56.7 ° and 9.8 ° respectively, demonstrating the surface is much more hydrophobic after PA intercalation. Rationally, this hydrophobic surface plays a decisive role in the inhibiting the decomposition/dissolution of VOPO_4 in aqueous electrolyte, thus leading to much improved long lifespan of the as-constructed

ZIBs. Most recently, Sun et al. reported that the decomposition/dissolution of $\text{VOPO}_4 \cdot 2\text{H}_2\text{O}$ can be prevented by PO_4^{3-} addition and high salt concentration of the aqueous electrolyte⁹. Such a strategy promotes a long-term cycling over 500 cycles with a stable capacity of only $90 \text{ mAh} \cdot \text{g}^{-1}$ at $2.0 \text{ A} \cdot \text{g}^{-1}$ but also increases the battery cost. In contrast, our strategy by PA-intercalation requires no addition of any reagent/salt addition, and realizes much superior cycling stability over 2000 cycles with a capacity of $\sim 200 \text{ mAh} \cdot \text{g}^{-1}$.

Discussion

In summary, we developed a controllable phenylamine-intercalated strategy for layered vanadium phosphates with various interlayer spacings (14.8 \AA , 15.6 \AA and 16.5 \AA). The crystal water in the $\text{VOPO}_4 \cdot 2\text{H}_2\text{O}$ was extracted from the interlayer space accompanied with the PA intercalation. The specific capacity is quite dependent on *d*-spacing in PA-VOP system followed by an approximate linear tendency, and the interlayer spacing (16.5 \AA) results in a maximum capacity of $268.2 \text{ mAh} \cdot \text{g}^{-1}$ at $0.1 \text{ A} \cdot \text{g}^{-1}$ and an energy density of $328.5 \text{ Wh} \cdot \text{Kg}^{-1}$. Both of the experimental data and theoretical calculation identify that the enlarged spacing can boost fast Zinc-ion diffusion with an ultrahigh diffusion coefficient of $\sim 5.7 \times 10^{-8} \text{ cm}^2 \cdot \text{s}^{-1}$. The intercalation of PA molecules also significantly increases the hydrophobicity in the aqueous electrolyte, inhibiting the decomposition/dissolution of $\text{VOPO}_4 \cdot 2\text{H}_2\text{O}$ and remarkably improved long-term cycling stability over 2000 cycles at $5.0 \text{ A} \cdot \text{g}^{-1}$ with a capacity of $\sim 200 \text{ mAh} \cdot \text{g}^{-1}$. Our study provides a feasible solution on the sluggish Zn^{2+} diffusion kinetics and poor stability of layered $\text{VOPO}_4 \cdot 2\text{H}_2\text{O}$, and also shows a clear understanding on the interlayer chemistry towards aqueous Zinc-ion storage. Similar strategy may be extended to other layered inorganic compounds with superior ion diffusion kinetics and better battery performance.

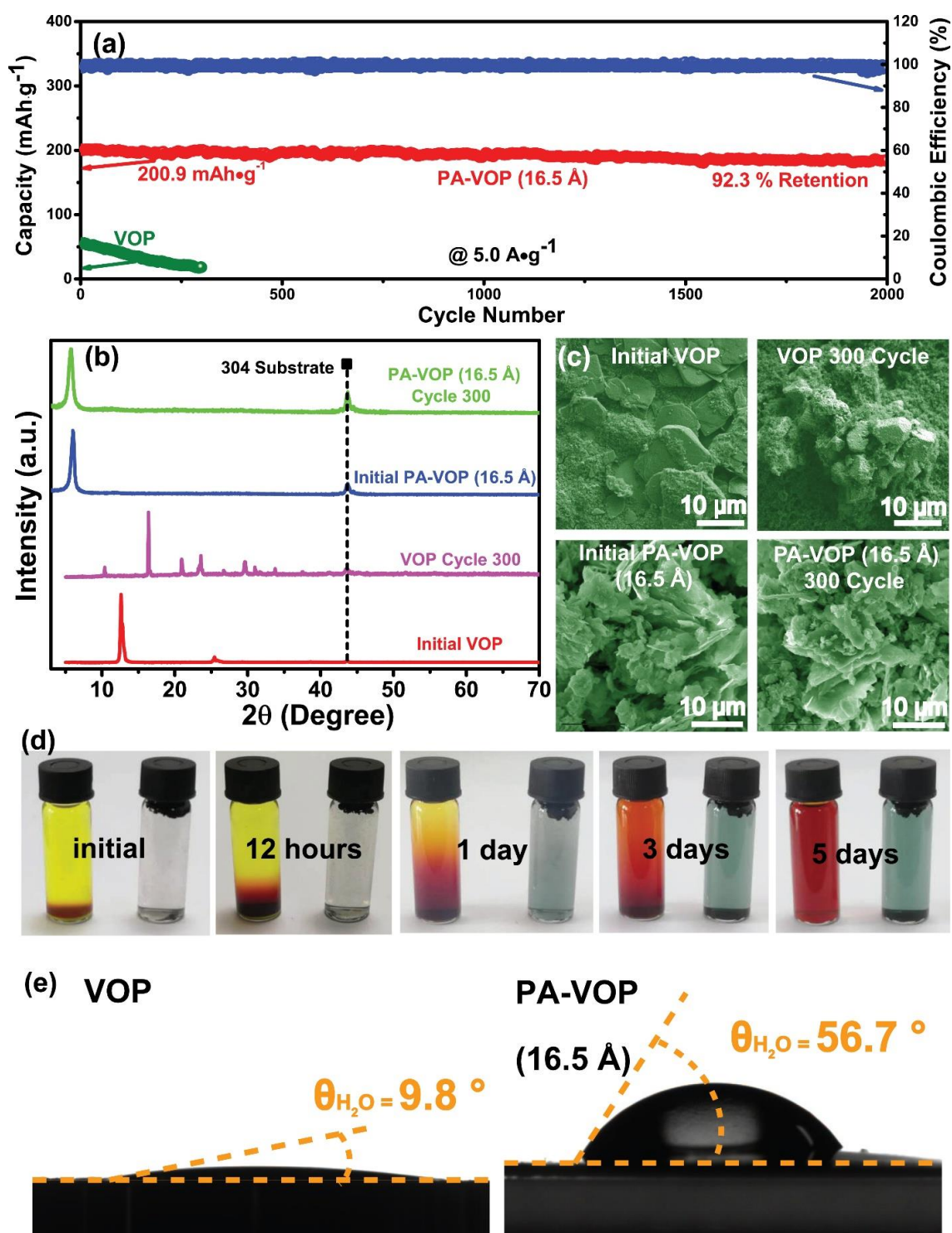


Fig. 5 Hydrophobicity improvement. **a** Long-term cycle test of Zn // VOP and Zn // PA-VOP (16.5 Å phase) battery using 2M $\text{Zn}(\text{CF}_3\text{SO}_3)_2$ aqueous electrolyte. **b** XRD patterns and **c** SEM images of the VOP and PA-VOP (16.5 Å phase) cathode before and after 300 cycles, respectively. **d** Optical photographs of the as-dispersed VOP and PA-VOP (16.5 Å phase) powder in 2M ZnSO_4 aqueous electrolyte at different times. **e** Water-based angle contact experiment of VOP and PA-VOP (16.5 Å phase) powder.

Methods

Materials synthesis. $\text{VOPO}_4 \cdot 2\text{H}_2\text{O}$ sample is synthesized based on a reported refluxing method with some modifications. Typically, 4.8 g V_2O_5 , 26.6 mL H_3PO_4 and 115.4 mL DI water is added to a three-necked flask, respectively, followed by 30 min of magnetic stirring with the addition of 10 mL of HNO_3 to stabilize the oxidation state of vanadium. The mixture is then heated at 110 °C for 16 h. Yellow precipitate is collected from the bottom after cooling down to room temperature, the yellow precipitate is collected by centrifugation, washed with DI water and acetone for 3 times, respectively. The resulting bright yellow VOP sample was dried at 60 °C in the vacuum oven. To introduce phenylamine molecules into the interlayer spacing of VOP, 0.3 g of as-synthesized VOP is mixed with 30 mL of isopropanol in 50 mL Teflon-lined strain-less steel autoclave and followed by the addition of 5 mL phenylamine. The mixture is stirred for 15 min and then heated in an oven at 60 °C for a short time (60, 90 and 120 min) to obtain phenylamine intercalated VOPO_4 (PA-VOP) with varied interlayer spacing (14.8, 15.6 and 16.5 Å), respectively. The black brown sediment in the bottom is then collected and washed with ethanol for 3 times. The PA-VOP powder is finally obtained after vacuum drying at 60 °C for 6h.

Materials characterization. The structure morphology and structure characterization are characterized by scanning electron microscopy (SEM, Phenom Pro X), transmission electron microscopy (TEM, Philips CM 200 FEG Field Emission Microscope) and X-ray diffraction (XRD, Bruker D8-A25 diffractometer using $\text{Cu K}\alpha$ radiation ($\lambda = 1.5406 \text{ \AA}$)). The high resolution transmission electron microscopy (HRTEM) and energy dispersive spectrum mapping (EDS-Mapping) is carried along with the TEM measurement to gather the detailed information of phase structure and chemical element distribution of the sample, respectively. Further information of the chemical bonding and microscopic condition is revealed by means of Fourier transform infrared spectroscopy (FTIR, BRUKER TENSOR II) and thermogravimetric analysis (TGA, SDT Q600), respectively. Water-based angle contact experiment (JY-82) is developed based on pressed powder of PA-VOP and VOP samples. Electronic conductivity test is carried out on a four-probe conductivity tester (ST2253y).

Electrochemical measurement. PA-VOP and VOP based cathodes of aqueous ZIBs is severally fabricated by mixing as-prepared samples, acetylene black and polyvinylidene fluoride (PVDF) on the basis of a mass ratio of 7:2:1 with the addition of 1-methyl-2-pyrrolidinone (NMP), then the uniform slurry is coated onto a piece of 304 stainless steel foil and drying at 100 °C for 12 h in a vacuum oven.

The slurry-coated foil is cut into $\Phi 15$ mm electrode as cathode, while the zinc foil washed with ethanol and glass fiber membrane is used as the anode and separator, respectively, and 2M $\text{Zn}(\text{CF}_3\text{SO}_3)_2$ is prepared as the electrolyte. The CR-2032 cell was assembled in air using the beforehand electrodes and other relevant components. LAND battery test system (CT2001A) was employed to evaluate the electrochemical performance of the battery: galvanostatic charge-discharge (GCD), rate capability and long-term cycle performance. Cyclic voltammetry (CV) test at different scan rate is performed on electrochemical workstation (CHI660E). Galvanostatic intermittent titration technique (GITT) is performed under a modified GCD mode, in which an operation period includes two parts: a charge / discharge procedure last for 10 min at $0.05 \text{ A} \cdot \text{g}^{-1}$ and a followed pause time for 10 min.

Fabrication of the flexible all-solid-state battery. The quasi solid flexible zinc-ion battery was fabricated using aforementioned slurry-coated carbon fiber cloth (CFC) as the cathode (mass loading: $2 \text{ mg} \cdot \text{cm}^{-2}$), CFC with a layer of zinc electrodeposited coating as the anode, a piece of filter paper as the separator and 2M $\text{Zn}(\text{ClO}_4)_2$ @ polyvinyl alcohol (PVA) as the electrolyte. The electrolyte was prepared by adding 3 g PVA to 30 mL 2M $\text{Zn}(\text{ClO}_4)_2$ aqueous solution little by little with continuous stirring, followed by oil bath treatment at $80 \text{ }^\circ\text{C}$ for 2h and gathering the thick sample when it came to the room temperature. The electrochemical deposition of zinc layer on the CFC was executed on CHI660E using potentiostatic model at -0.7 V (vs. $\text{Zn}^{2+} / \text{Zn}$) for 2000 s. The ultimate flexible all-solid-state battery was assembled and sealed with polyimide (PI) film to form a stable sandwich structure.

Electrochemical calculation method. The calculation method for capacity contribution of the cathodes is based on the following equation:

$$I_p = C_1 v + C_2 v^{\frac{1}{2}} \quad (1)$$

where I_p ($\text{A} \cdot \text{g}^{-1}$) is the peak current density at different scan rate, v ($\text{mV} \cdot \text{s}^{-1}$) is the specific scan rate, C_1 and C_2 are the corresponding constant factors of the capacity contribution of surface pseudocapacitive effect and battery-type effect, respectively.

With a deformation of the above equation, the specific contribution rate of different internal mechanisms can be solved according to the following equation:

$$\frac{I_p}{v^{\frac{1}{2}}} = C_1 v^{\frac{1}{2}} + C_2 \quad (2)$$

The specific energy density ($\text{Wh} \cdot \text{kg}^{-1}$) and average specific power density ($\text{W} \cdot \text{kg}^{-1}$) of the batteries is calculated in terms of the following equations:

$$E_s = \int_{V_0}^{V_1} C_s(V) \quad (3)$$

$$P_s = \frac{E_s}{t} \quad (4)$$

Where E_s is the calculated specific energy density ($\text{Wh}\cdot\text{kg}^{-1}$), P_s is the average specific power density ($\text{W}\cdot\text{kg}^{-1}$); C_s ($\text{mAh}\cdot\text{g}^{-1}$) is the specific capacity of the battery, V_0 and V_1 is the voltage lower limit and voltage upper limit of discharge procedure, respectively, and t is the discharge time (h). All the parameters calculated are based on the mass loading of the active materials (VOP or PA-VOP).

Diffusion coefficient ($D_{\text{Zn}^{2+}}$) of Zinc-ion can be experimentally calculated by GITT method in terms of the following equation:

$$D = \frac{4}{\pi\tau} L^2 \left(\frac{\Delta E_s}{\Delta E_t} \right)^2 \quad (5)$$

Where D is the diffusion coefficient of Zinc-ion, τ is the relaxation time of current pulse, L is diffusion length which is approximate to the thickness of coated slurry, ΔE_s and ΔE_t is the voltage change produced by current pulse and the galvanostatic charge / discharge, respectively.

Simulation details. The modeling in this study was performed in the framework of the DFT as implemented in the Vienna Ab initio Simulation Package (VASP). The functional of Perdew-Burke-Ernzerhof based on generalized gradient approximation (GGA) was applied to describe the exchange-correlation energy. In addition, the zero damping DFT-D3 dispersion correction method of Grimme was accounted for VdW interaction in the system. A vacuum space of 15 Å was adopted. The plane-wave cutoff energy was set to be 480 eV, and the k-mesh was determined to be $7 \times 7 \times 1$ according to the convergence test, which makes the energy accuracy within 1.0×10^{-3} eV atom^{-1} . Finally, a double-layered VOPO₄ model was constructed, with the corresponding interlayer spacing obtained from our previous XRD and HRTEM analysis, thereby the diffusion of zinc ion between VOPO₄ layers was simulated using the climbing-image nudged elastic band method.

Data Availability

The authors declare that all the relevant data are available within the paper and its Supplementary Information file or from the corresponding author on reasonable request.

References

- 1 Choi, J. W. & Aurbach, D. Promise and reality of post-lithium-ion batteries with high energy densities. *Nat. Rev. Mater.* **1** (2016).
- 2 Canepa, P. *et al.* Odyssey of Multivalent Cathode Materials: Open Questions and Future Challenges. *Chem. Rev.* **117**, 4287-4341 (2017).
- 3 Fang, G. Z., Zhou, J., Pan, A. Q. & Liang, S. Q. Recent Advances in Aqueous Zinc-ion Batteries. *ACS Energy Lett.* **3**, 2480-2501 (2018).
- 4 Konarov, A. *et al.* Present and Future Perspective on Electrode Materials for Rechargeable Zinc-ion Batteries. *ACS Energy Lett.* **3**, 2620-2640 (2018).
- 5 Pang, Q. *et al.* H₂V₃O₈ Nanowire / Graphene Electrodes for Aqueous Rechargeable Zinc Ion Batteries with High Rate Capability and Large Capacity. *Adv. Energy Mater.* **8**, 1800144 (2018).
- 6 Li, H. F. *et al.* MoS₂ nanosheets with expanded interlayer spacing for rechargeable aqueous Zn-ion batteries. *Energy Storage Mater.* **19**, 94-101 (2019).
- 7 Wang, F. *et al.* How Water Accelerates Bivalent Ion Diffusion at the Electrolyte / Electrode Interface. *Angew. Chem. Int. Ed.* **57**, 11978-11981 (2018).
- 8 Wan, F. *et al.* Reversible Oxygen Redox Chemistry in Aqueous Zinc-ion Batteries. *Angew. Chem. Int. Ed.* **58**, 7062-7067 (2019).
- 9 Shi, H. Y. *et al.* Inhibiting VOPO₄·xH₂O Decomposition and Dissolution in Rechargeable Aqueous Zinc Batteries to Promote Voltage and Capacity Stabilities. *Angew. Chem. Int. Ed.* **58**, 16057-16061 (2019).
- 10 Wu, Z. Y. *et al.* Novel Sub-5 nm Layered Niobium Phosphate Nanosheets for High-Voltage, Cation-Intercalation Typed Electrochemical Energy Storage in Wearable Pseudocapacitors. *Adv. Energy Mater.* **9**, 1900111 (2019).
- 11 Wu, C. Z. *et al.* Two-dimensional vanadyl phosphate ultrathin nanosheets for high energy density and flexible pseudocapacitors. *Nat. Commun.* **4**, 2431 (2013).
- 12 Huang, J. H. *et al.* Polyaniline-intercalated manganese dioxide nanolayers as a high-performance cathode material for an aqueous zinc-ion battery. *Nat. Commun.* **9**, 2906 (2018).
- 13 Han, M. H., Gonzalo, E., Singh, G. & Rojo, T. A comprehensive review of sodium layered oxides: powerful cathodes for Na-ion batteries. *Energy Environ. Sci.* **8**, 81-102 (2015).

- 14 Wang, G. *et al.* Vertically Aligned MoS₂ Nanosheets Patterned on Electrochemically Exfoliated Graphene for High-Performance Lithium and Sodium Storage. *Adv. Energy Mater.* **8**, 1702254 (2018).
- 15 Mao, M. L., Gao, T., Hou, S. Y. & Wang, C. S. A critical review of cathodes for rechargeable Mg batteries. *Chem. Soc. Rev.* **47**, 8804-8841 (2018).
- 16 Ji, X. *et al.* Water-Activated VOPO₄ for Magnesium Ion Batteries. *Nano Lett.* **18**, 6441-6448 (2018).
- 17 Yang, Y. Q. *et al.* Li⁺ intercalated V₂O₅·nH₂O with enlarged layer spacing and fast ion diffusion as an aqueous zinc-ion battery cathode. *Energy Environ. Sci.* **11**, 3157-3162 (2018).
- 18 Zhou, L. M. *et al.* Interlayer-Spacing-Regulated VOPO₄ Nanosheets with Fast Kinetics for High-Capacity and Durable Rechargeable Magnesium Batteries. *Adv. Mater.* **30**, 1801984 (2018).
- 19 de Farias, R. F. & Airoidi, C. Synthesis and characterization of an VOPO₄-polyaniline lamellar hybrid compound. *Solid State Sci.* **5**, 611-613 (2003).
- 20 Kinomura, N., Toyama, T. & Kumada, N. Intercalative Polymerization of Aniline in VOPO₄·2H₂O. *Solid State Ionics* **78**, 281-286 (1995).
- 21 Zampronio, E. C. & Oliveira, H. P. Synthesis, spectroscopic and structural characterization of poly-o-methoxyaniline and poly-o-methylaniline intercalated into layered vanadyl phosphate. *Mater. Res. Bull.* **39**, 1525-1538 (2004).
- 22 Wu, Z. Y. *et al.* A Layered Zn_{0.4}VOPO₄·0.8H₂O Cathode for Robust and Stable Zn Ion Storage. *ACS Appl. Energy Mater.* **3**, 3919-3927 (2020).
- 23 Verma, V. *et al.* Layered VOPO₄ as a Cathode Material for Rechargeable Zinc-ion Battery: Effect of Polypyrrole Intercalation in the Host and Water Concentration in the Electrolyte. *ACS Appl. Energy Mater.* **2**, 8667-8674 (2019).
- 24 Kundu, D., Adams, B. D., Duffort, V., Vajargah, S. H. & Nazar, L. F. A high-capacity and long-life aqueous rechargeable zinc battery using a metal oxide intercalation cathode. *Nat. Energy* **1**, 16119 (2016).
- 25 Xia, C. *et al.* Rechargeable Aqueous Zinc-ion Battery Based on Porous Framework Zinc Pyrovanadate Intercalation Cathode. *Adv. Mater.* **30**, 1705580 (2018).
- 26 He, P. *et al.* Layered VS₂ Nanosheet-Based Aqueous Zn Ion Battery Cathode. *Adv. Energy Mater.* **7**, 1601920 (2017).

- 27 Alfaruqi, M. H. *et al.* A layered delta-MnO₂ nanoflake cathode with high zinc-storage capacities for eco-friendly battery applications. *Electrochem. Commun.* **60**, 121-125 (2015).
- 28 Wu, Z. Y. *et al.* Ultrathin VSe₂ Nanosheets with Fast Ion Diffusion and Robust Structural Stability for Rechargeable Zinc-ion Battery Cathode. *Small* **16**, 2000698 (2020).
- 29 Shi, H. Y., Ye, Y. J., Liu, K., Song, Y. & Sun, X. Q. A Long-Cycle-Life Self-Doped Polyaniline Cathode for Rechargeable Aqueous Zinc Batteries. *Angew. Chem. Int. Ed.* **57**, 16359-16363 (2018).
- 30 Ghanbari, K., Mousavi, M. F., Sharnsipur, M. & Karami, H. Synthesis of polyaniline / graphite composite as a cathode of Zn-polyaniline rechargeable battery. *J. Power Sources* **170**, 513-519 (2007).
- 31 Karami, H., Mousavi, M. F. & Shamsipur, M. A new design for dry polyaniline rechargeable batteries. *J. Power Sources* **117**, 255-259 (2003).
- 32 Zhang, H. Z. *et al.* Interlayer Engineering of alpha-MoO₃ Modulates Selective Hydronium Intercalation in Neutral Aqueous Electrolyte. *Angew. Chem. Int. Ed.* **60**, 896-903 (2021).
- 33 Ding, J. W. *et al.* Ultrafast Zn²⁺ Intercalation and Deintercalation in Vanadium Dioxide. *Adv. Mater.* **30**, 1800762 (2018).
- 34 Yan, M. Y. *et al.* Water-Lubricated Intercalation in V₂O₅·nH₂O for High-Capacity and High-Rate Aqueous Rechargeable Zinc Batteries. *Adv. Mater.* **30**, 1703725 (2018).
- 35 Kundu, D. *et al.* Aqueous vs. nonaqueous Zn-ion batteries: consequences of the desolvation penalty at the interface. *Energy Environ. Sci.* **11**, 881-892 (2018).
- 36 Soundharrajan, V. *et al.* Na₂V₆O₁₆·3H₂O Barnesite Nanorod: An Open Door to Display a Stable and High Energy for Aqueous Rechargeable Zn-Ion Batteries as Cathodes. *Nano Lett.* **18**, 2402-2410 (2018).
- 37 Tang, B. Y. *et al.* Potassium vanadates with stable structure and fast ion diffusion channel as cathode for rechargeable aqueous zinc-ion batteries. *Nano Energy* **51**, 579-587 (2018).
- 38 Sambandam, B. *et al.* Aqueous rechargeable Zn-ion batteries: an imperishable and high-energy Zn₂V₂O₇ nanowire cathode through intercalation regulation. *J. Mater. Chem. A* **6**, 3850-3856 (2018).
- 39 Liu, S. C. *et al.* Tuning the Kinetics of Zinc-ion Insertion/Extraction in V₂O₅ by In Situ Polyaniline Intercalation Enables Improved Aqueous Zinc-ion Storage Performance. *Adv. Mater.* **32**, 2001113 (2020).

- 40 Jiang, B. Z. *et al.* Manganese Sesquioxide as Cathode Material for Multivalent Zinc Ion Battery with High Capacity and Long Cycle Life. *Electrochim. Acta* **229**, 422-428 (2017).
- 41 Zhang, N. *et al.* Cation-Deficient Spinel ZnMn_2O_4 Cathode in $\text{Zn}(\text{CF}_3\text{SO}_3)_2$ Electrolyte for Rechargeable Aqueous Zn-Ion Battery. *J. Am. Chem. Soc.* **138**, 12894-12901 (2016).
- 42 Liu, W. B. *et al.* Investigation of zinc ion storage of transition metal oxides, sulfides, and borides in zinc ion battery systems. *Chem. Commun.* **53**, 6872-6874 (2017).
- 43 Zhang, L. Y., Chen, L., Zhou, X. F. & Liu, Z. P. Towards High-Voltage Aqueous Metal-Ion Batteries Beyond 1.5 V: The Zinc / Zinc Hexacyanoferrate System. *Adv. Energy Mater.* **5**, 1400930 (2015).
- 44 Liu, Z., Pulletikurthi, G. & Endres, F. A Prussian Blue / Zinc Secondary Battery with a Bio-Ionic Liquid-Water Mixture as Electrolyte. *ACS Appl. Mater. Interfaces* **8**, 12158-12164 (2016).
- 45 Hou, Z. G. *et al.* Surfactant widens the electrochemical window of an aqueous electrolyte for better rechargeable aqueous sodium / zinc battery. *J. Mater. Chem. A* **5**, 730-738 (2017).
- 46 Li, G. L. *et al.* Towards polyvalent ion batteries: A zinc-ion battery based on NASICON structured $\text{Na}_3\text{V}_2(\text{PO}_4)_3$. *Nano Energy* **25**, 211-217 (2016).
- 47 Li, W., Wang, K. L., Cheng, S. J. & Jiang, K. A long-life aqueous Zn-ion battery based on $\text{Na}_3\text{V}_2(\text{PO}_4)_2\text{F}_3$ cathode. *Energy Storage Mater.* **15**, 14-21 (2018).
- 48 Zhao, J. W. *et al.* High-voltage Zn / $\text{LiMn}_{0.8}\text{Fe}_{0.2}\text{PO}_4$ aqueous rechargeable battery by virtue of "water-in-salt" electrolyte. *Electrochem. Commun.* **69**, 6-10 (2016).
- 49 Zhao, Q. *et al.* High-capacity aqueous zinc batteries using sustainable quinone electrodes. *Sci. Adv.* **4**, eaao1761 (2018).
- 50 Kundu, D. *et al.* Organic Cathode for Aqueous Zn-Ion Batteries: Taming a Unique Phase Evolution toward Stable Electrochemical Cycling. *Chem. Mater.* **30**, 3874-3881 (2018).
- 51 Nam, K. W. *et al.* Redox-Active Phenanthrenequinone Triangles in Aqueous Rechargeable Zinc Batteries. *J. Am. Chem. Soc.* **142**, 2541-2548 (2020).
- 52 Guo, Z. W. *et al.* An Environmentally Friendly and Flexible Aqueous Zinc Battery Using an Organic Cathode. *Angew. Chem. Int. Ed.* **57**, 11737-11741 (2018).
- 53 Ma, L. T. *et al.* Initiating a mild aqueous electrolyte Co_3O_4 / Zn battery with 2.2 V-high voltage and 5000-cycle lifespan by a Co(III) rich-electrode. *Energy Environ. Sci.* **11**, 2521-2530 (2018).

- 54 Lee, B. *et al.* Electrochemically-induced reversible transition from the tunneled to layered polymorphs of manganese dioxide. *Sci. Rep.* **4**, 6066 (2014).
- 55 Xu, C. J., Li, B. H., Du, H. D. & Kang, F. Y. Energetic Zinc Ion Chemistry: The Rechargeable Zinc Ion Battery. *Angew. Chem. Int. Ed.* **51**, 933-935 (2012).
- 56 Trocoli, R. & La Mantia, F. An Aqueous Zinc-ion Battery Based on Copper Hexacyanoferrate. *Chemsuschem* **8**, 481-485 (2015).
- 57 Gogotsi, Y. & Penner, R. M. Energy Storage in Nanomaterials - Capacitive Pseudocapacitive, or Battery-like? *ACS Nano* **12**, 2081-2083 (2018).
- 58 Yan, Y. *et al.* Understanding the fast lithium storage performance of hydrogenated TiO₂ nanoparticles. *J. Mater. Chem. A* **1**, 14507-14513 (2013).
- 59 Zhang, N. *et al.* Rechargeable Aqueous Zn-V₂O₅ Battery with High Energy Density and Long Cycle Life. *ACS Energy Lett.* **3**, 1366-1372 (2018).
- 60 Yao, S. S. *et al.* Ultrathin Sb₂S₃ nanosheet anodes for exceptional pseudocapacitive contribution to multi-battery charge storage. *Energy Storage Mater.* **20**, 36-45 (2019).
- 61 Jiang, L. *et al.* Ultrafast Zinc-ion Diffusion Ability Observed in 6.0-Nanometer Spinel Nanodots. *ACS Nano* **13**, 10376-10385 (2019).
- 62 Yang, F. H. *et al.* Ultrathin Few-Layer GeP Nanosheets via Lithiation-Assisted Chemical Exfoliation and Their Application in Sodium Storage. *Adv. Energy Mater.* **10**, 1903826 (2020).

Acknowledgements

This work was financially supported by the National Natural Science Foundation of China (Nos.51872051, 51731004, 51701042), the Science and Technology Committee of Shanghai Municipality (18520723100), the Researching Program of State Grid Corporation of China (GYW17201800011).

Author contributions

L. F. H. supervised the project. L. F. H., Z. Y. W. designed the sample preparation and executed the electrochemical screening experiments. C. J. L. performed DFT calculations and simulations. F. Y. participated in the battery performance measurement and analysis. Y. L. and

R. L. P. conducted material characterizations on SEM, TEM, XRD, XAS, Raman characterizations. Z. M. S. discussed the results and interpreted the data. All authors contributed to the writing of the paper.

Competing interests

The authors declare no competing interests.

Figures

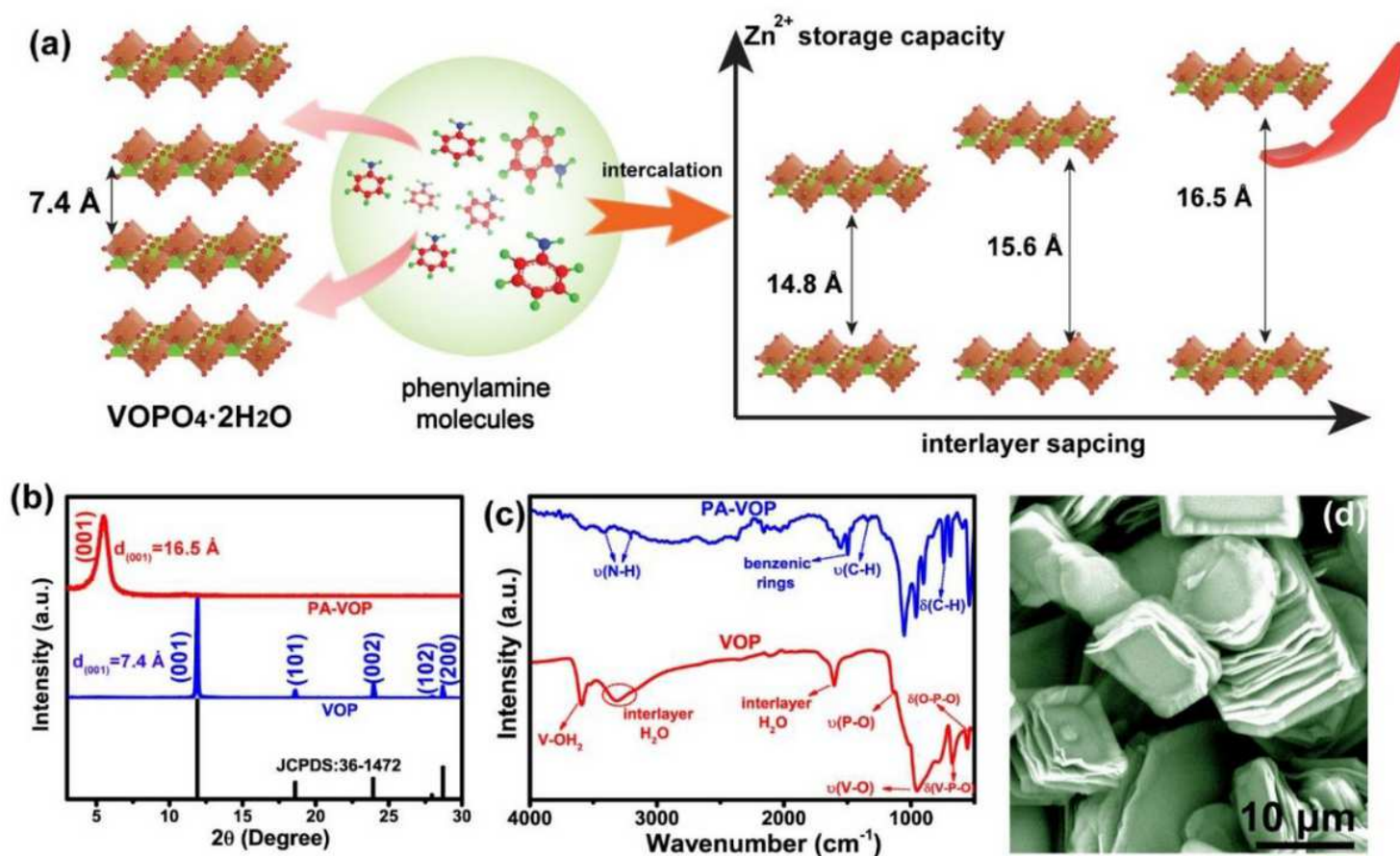


Figure 1

Controllable PA intercalation in layered $\text{VOPO}_4 \cdot 2\text{H}_2\text{O}$. a Scheme of capacity regulation for Zinc-ion storage via PA-intercalation engineering. b Powder XRD patterns and c FTIR spectra of VOP and PA-VOP samples, respectively. d Typical SEM image of PA-VOP (16.5 Å phase) .

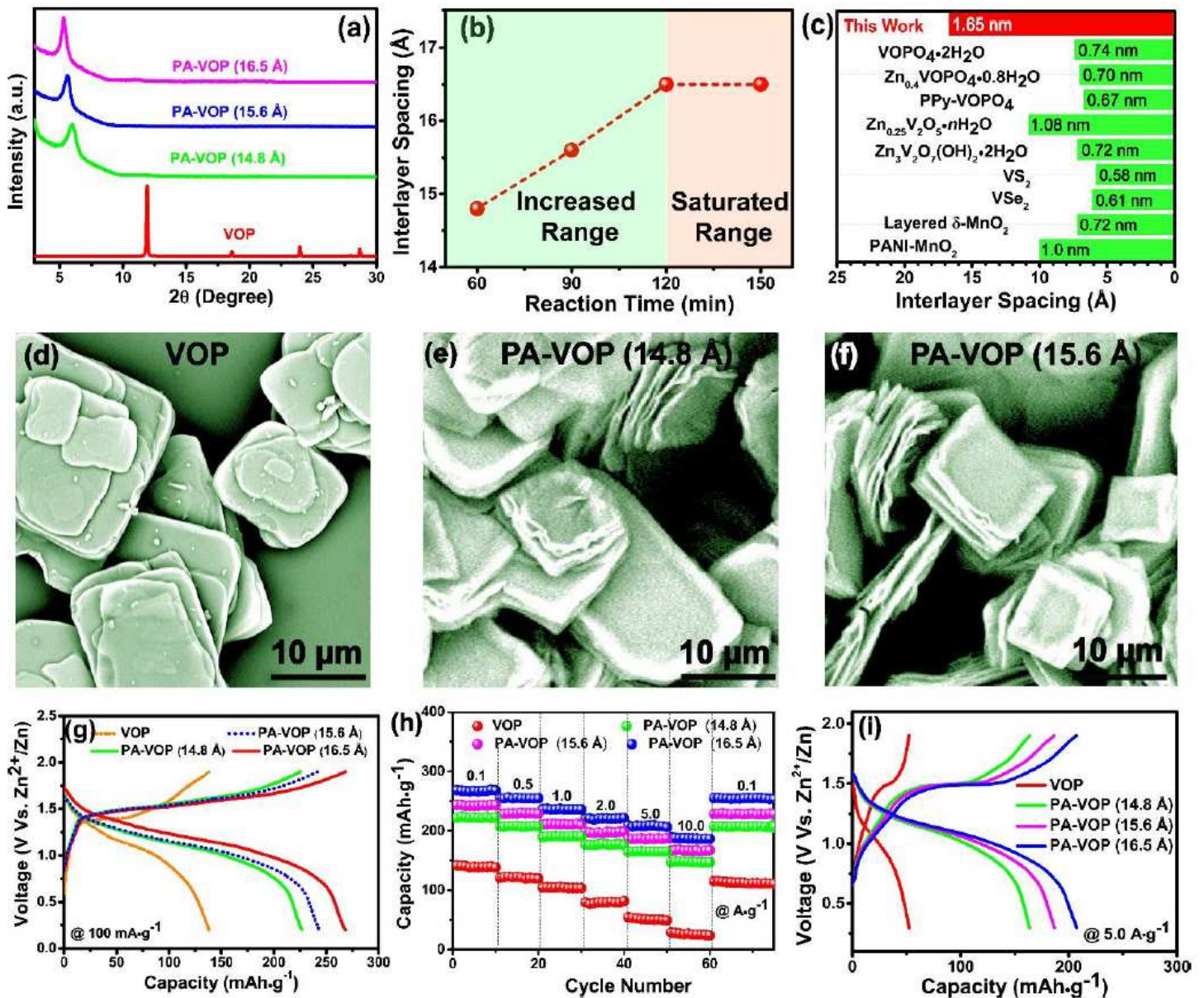


Figure 2

Interlayer spacing dependent battery performance. a XRD patterns of various PA-VOP samples synthesized under different temperature and solvent. b Dependence of interlayer spacing and solvothermal time. c Typical layered materials served as cathode of aqueous ZIBs.^{7,12,22-28} d-f SEM image of VOP, PA-VOP (14.8 Å phase) and PA-VOP (15.6 Å phase) samples, respectively. g GCD curves of VOP based ZIB and PA-VOP based ZIBs with adjustable interlayer spacing, respectively (14.8, 15.6 and 16.5 Å). h Cycle test at varied current density of VOP and PA-VOP cathodes with different interlayer spacing, severally. i GCD curves of VOP and PA-VOP cathode with different interlayer spacing at a current density of 5 A·g⁻¹, respectively.

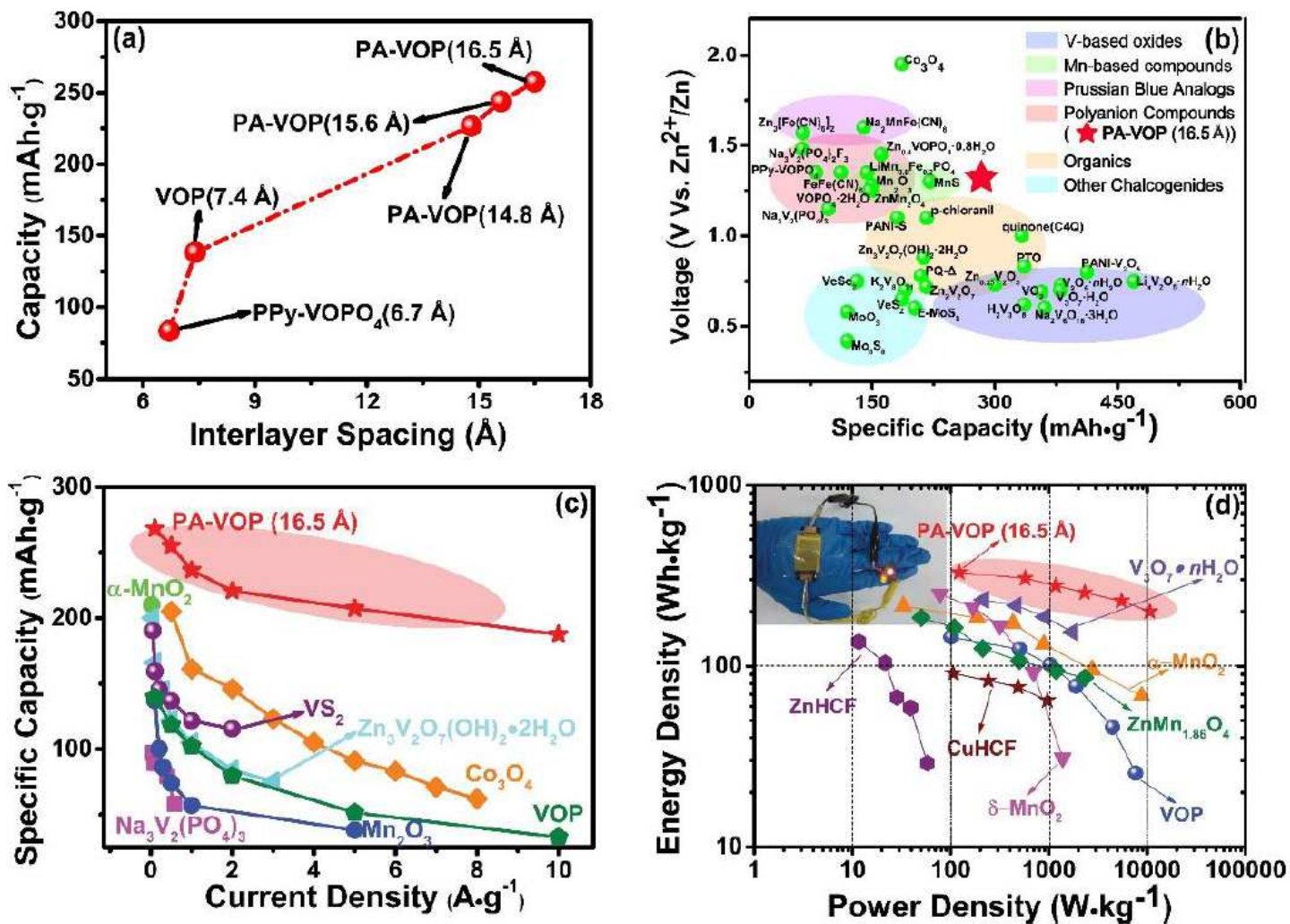


Figure 3

Performance comparison. a Dependence of specific capacity and interlayer spacing of various VOPO₄-based cathodes at the current density of 0.1 A·g⁻¹.²³ b Voltage plateau versus specific capacity for various mainstream cathodes recently reported and our PA-VOP (16.5 \AA) cathode.^{5-7,17,22-26,33-53} c Comparison of the rate-capacity between our PA-VOP cathode and the other recently reported cathodes for aqueous ZIBs.^{25,40,46,53-54} d Ragone plot of PA-VOP cathode and a series of other cathode materials reported previously.^{27,35,41,43,55-56} Insert is a solid-state battery constructed from the PA-VOP @ CFC cathode driving a group of LEDs.

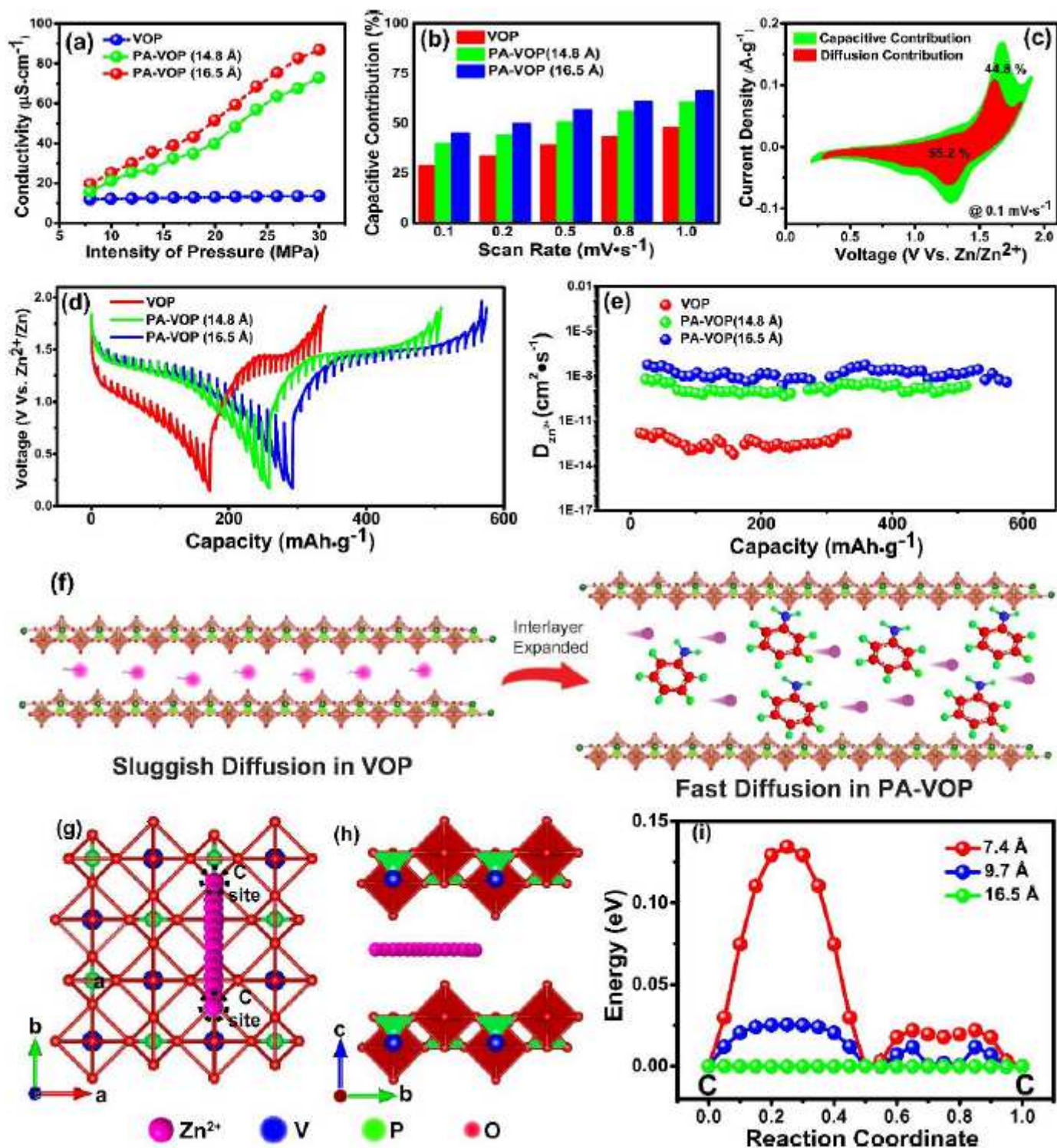


Figure 4

Reaction/diffusion kinetics mechanism. a Electronic conductivity test under different pressure. b Capacitive contribution of VOP, PA-VOP (14.8 Å phase) and PA-VOP (16.5 Å phase), respectively. c CV curve containing the schematic of capacitive and diffusion contribution of PA-VOP (16.5 Å phase) cathode at the scan rate of $0.1 \text{ mV}\cdot\text{s}^{-1}$ d GITT curve and e the calculated diffusion coefficient of VOP, PA-VOP (14.8 Å phase) and PA-VOP (16.5 Å phase), respectively. f Schematic illustration of Zn^{2+} diffusion

kinetics in PA-VOP and VOP cathode. g Zinc-ion diffusion path scheme in top view and h side view mode. i Calculated energy barrier curve of the PA-VOP samples with different interlayer spacing.

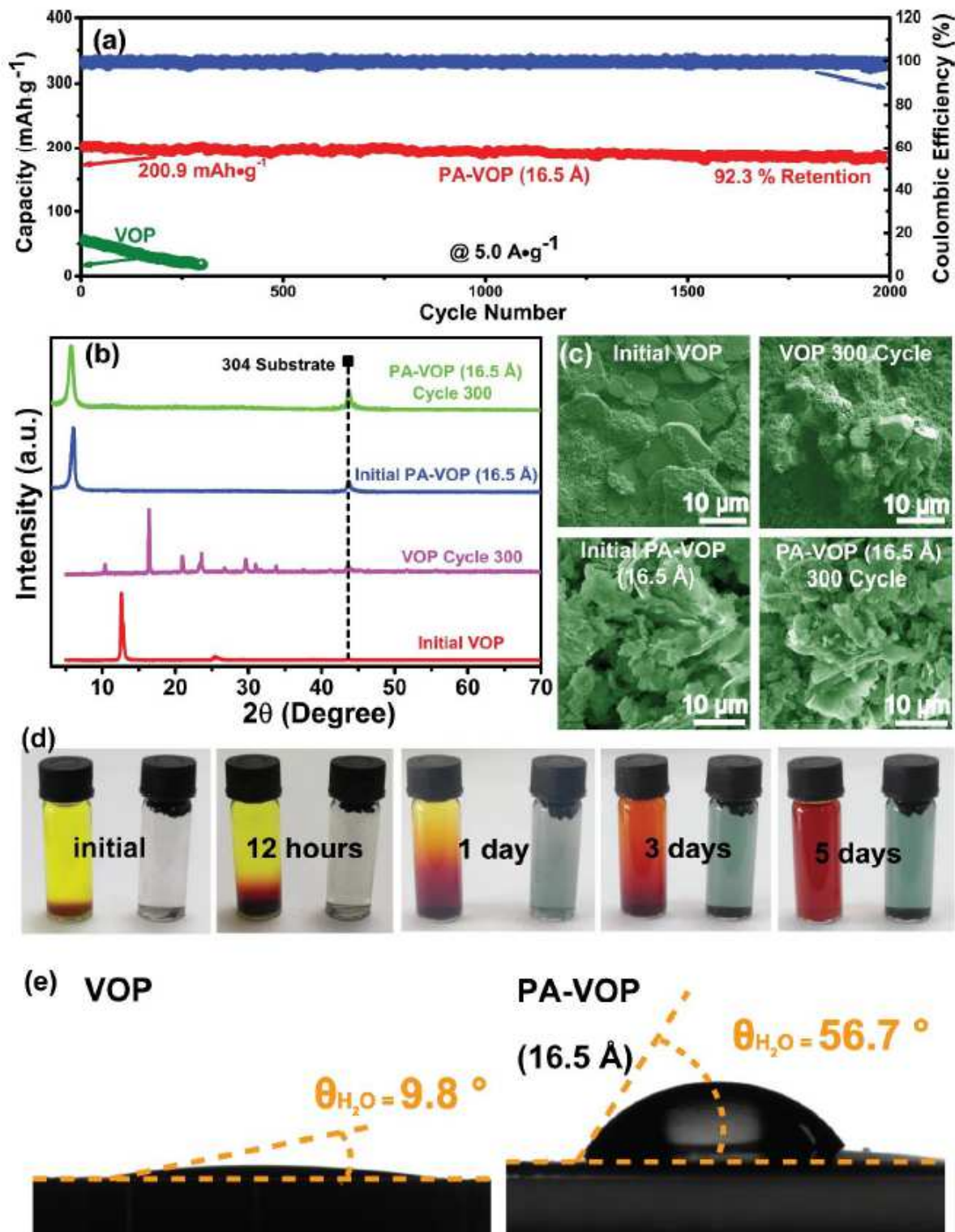


Figure 5

Hydrophobicity improvement. a Long-term cycle test of Zn // VOP and Zn // PA-VOP (16.5 Å phase) battery using 2M Zn(CF₃SO₃)₂ aqueous electrolyte. b XRD patterns and c SEM images of the VOP and PA-VOP (16.5 Å phase) cathode before and after 300 cycles, respectively. d Optical photographs of the as-

dispersed VOP and PA-VOP (16.5 Å phase) powder in 2M ZnSO₄ aqueous electrolyte at different times. e
Water-based angle contact experiment of VOP and PA-VOP (16.5 Å phase) powder.

Supplementary Files

This is a list of supplementary files associated with this preprint. Click to download.

- [SupplementaryFile.pdf](#)